Chapter 7. An experimental and numerical analysis for fatigue strength characterization and life prediction of giant magnetostrictive material

7.1. Introduction

Giant magnetostrictive materials (GMM) exhibit nonlinear magneto-thermo-elastic coupling phenomena and possess some attractive properties as high saturation magnetostriction, variable elastic modulus, high curie temperature and faster response to operational factors, thereby finding potential applications in intelligent devices [1–3] [4,5]. However, this attractiveness comes at a price, as Terfenol-D is a costly and difficult-to-manufacture alloy due to the high reactivity of the elements and impurities that comprise it [18,19]. The biggest drawback of Terfenol-D is its extremely brittle characteristics, and has a substantially lower tensile strength than its compressive strength in the presence of manufacturing flaws such as cracks, cavities, inclusions, de-bonding, and dislocations [20]. These manufacturing flaws may lead to critical crack propagation and ultimately mechanical failure of intelligent devices. At present, giant magnetostrictive material based intelligent devices are popularly used in industries such as automotive, avionics, and construction engineering. For example, Terfenol-D actuators are used in parallel to helicopter gearbox support strut to attenuate the kinetic energy by 30-40 dB on the fuselage connection side as shown in **Figure 1.3** and thereby reduce the excessive noise inside the chopper and pilot fatigue. **Figure 1.4** shows a gear box assembly incorporating two pair of Terfenol-D actuators around the driving shaft to attenuate the gearbox vibrations and subsequently minimizes the wide range of audible and tangible discomfort. Thus, the dynamic forces generated by such industrial applications could lead to undesired operating circumstances and structural vibrations in intelligent devices and affecting their service life.

The long-term service life of giant magnetostrictive material (e.g., Terfenol-D) is one of the primary concerns in many industries that prevents the widespread application of magnetostrictive devices, especially when subjected to external magnetic field with cyclic loading environment. Because of high brittleness, low tensile strength, manufacturing flaws, and undesirable operating circumstances; the Terfenol-D based smart sensing devices are susceptible to in-service fatigue-fracture failure in the presence of a magnetic field. As a result, it is critical to analyze the performance of GMMs under such circumstances and to provide a method for estimating magnetostrictive device service life.

This chapter presents an experimental and numerical investigation of the cyclic fatigue behaviour of the pre-cracked giant magnetostrictive material (i.e., Terfenol-D). Then it proposes a method to estimate the service life of the giant magnetostrictive material. It constitutes exclusive magneto-elastic cyclic flexure experiments on the three-point SENB specimens and finite element analyses to investigate the fatigue-fracture parameters of the bi-nonlinear Terfenol-D. The fatigue experiments are performed in two stages in presence and absence of external magnetic field as per ASTM standards (i.e., E399 and E 647). In first stage, specimens are tested in cyclic fatigue loading to capture the fatigue crack growth data with number of spent cycles. In second stage, the specimens are tested in cyclic fatigue loading up to fracture. The digital image correlation technique is used to capture the fatigue crack growth data with number of spent cycles. A two-dimensional J-integral definition for determining the strain energy release rate has also been used as described in Chapter 4, which is subsequently used to characterize the crack front singularity near the fracture process zone. A plane strain finite element analyses employing a vector generalized nonlinear hysteretic magneto-thermo-elastic constitutive model as proposed in Chapter 3 [127] have been conducted to evaluate the strain energy release rate of the Terfenol-D SENB specimen under an applied external magnetic field. The calibrated material parameters from Chapter 5 have

been employed in the finite element procedures. Further, the updated Paris law constants [99–101] (as described in Eq. (2.44)) from the correlation of the crack growth rate with the values of ΔJ with the help of the fatigue crack growth vs number of spent cycles data (i.e., stage I experiment) is determined for a set of load ratio, magnetic field, and cyclic frequency. The experimentally evaluated fatigue failure data with the number of cycles spent (i.e., stage II experiment) were then compared with the numerical prediction of fatigue life to determine the validation and relevance of evaluated Paris law constants. Finally, the necessity and significance of considering the bi-nonlinear strain energy release rate, influenced by the coupled magneto-elastic field, were discussed for fatigue crack propagation with validating the observations.

7.2. Fatigue experiment

A three-point bend flexure fatigue test is performed to characterize the fatigue parameters and life of giant magnetostrictive material (i.e., Terfenol-D) in the coupled magneto-elastic field, which is procured from Lanzhou Jian Xing Commercial and Trading Co., Ltd. in cuboid bar shapes with a cross-section of $3.5 \times 3.5\ \mathrm{mm}^2$, respectively. **Figure 7.1** shows the experimental setup for the fatigue strength characterization of single edge notch bend (SENB) specimen in three-point loading under magnetic field with dynamic UTM INSTRON 8801 similar to quasistatic three-point bend test as described in section 6.2. The cyclic fatigue tests are performed on Terfenol-D SENB specimens under the externally applied magnetic fields in accordance with ASTM E399-20a [131], E1820-18a [132], E 647[136] and E739 [137] and the impact of bi-nonlinear elasticity and magnetic field on the fatigue-fracture properties have been experimentally investigated. For the test, nonmagnetic bending fixtures made of steel 316 are used as described in section 6.2.

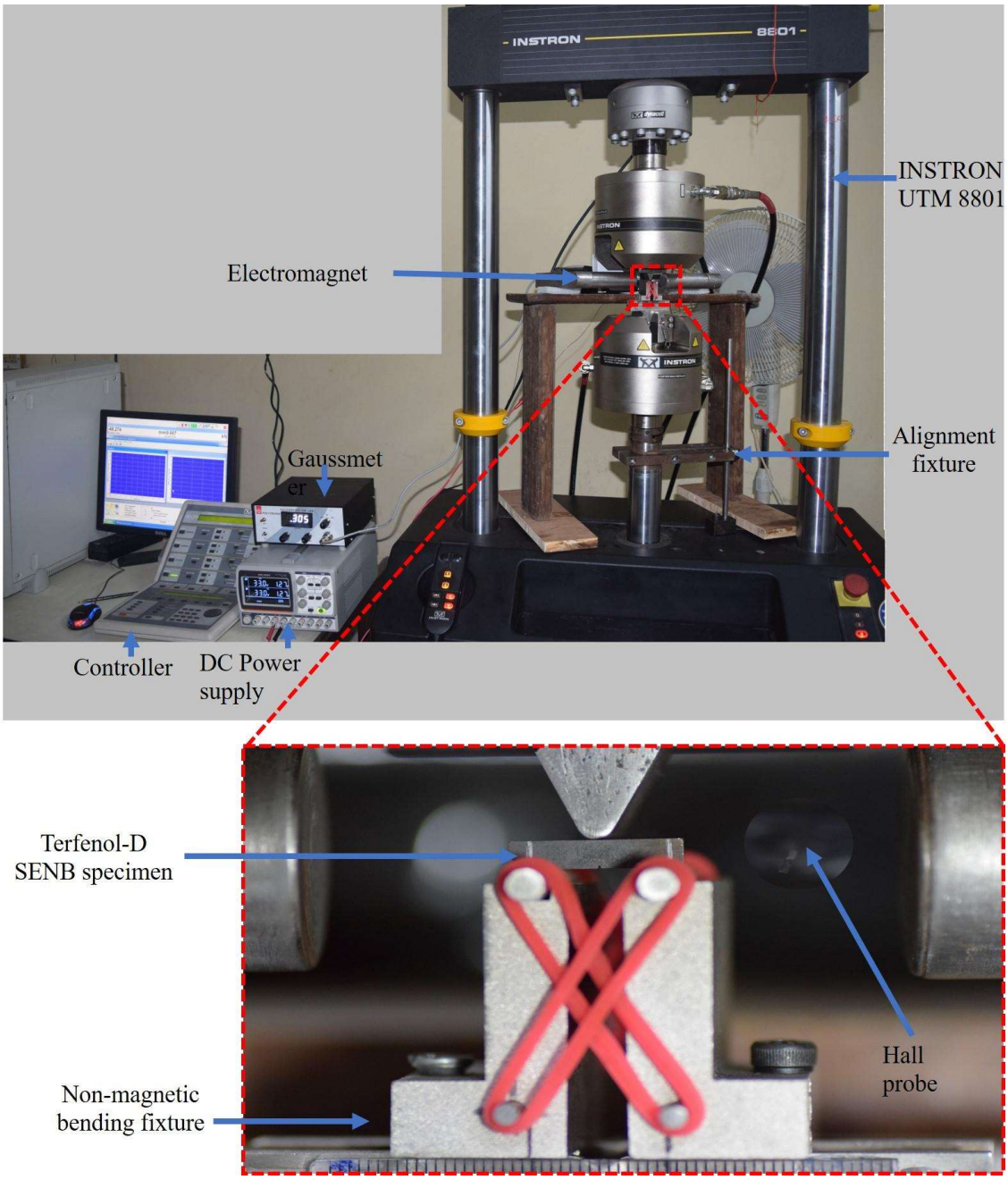

Figure 7.1: Experimental setup for fatigue strength characterization of single edge notch bend (SENB) specimen in three-point loading under magnetic field

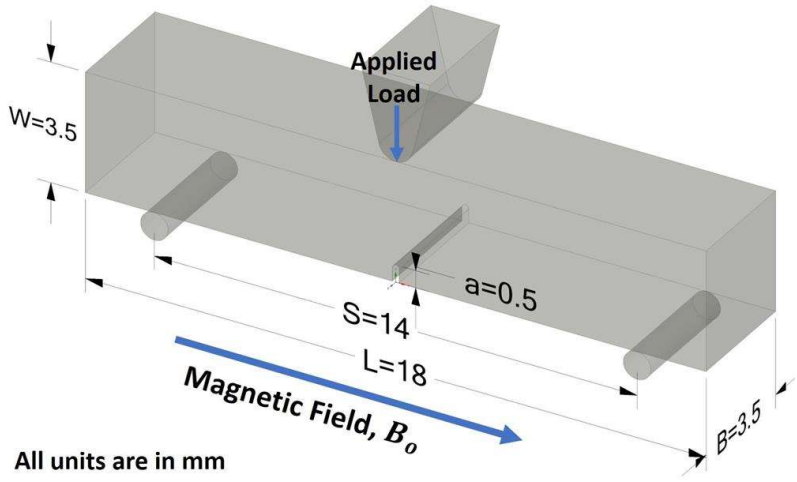

Figure 7.2: Specimens geometry as per ASTM E399-18a standard

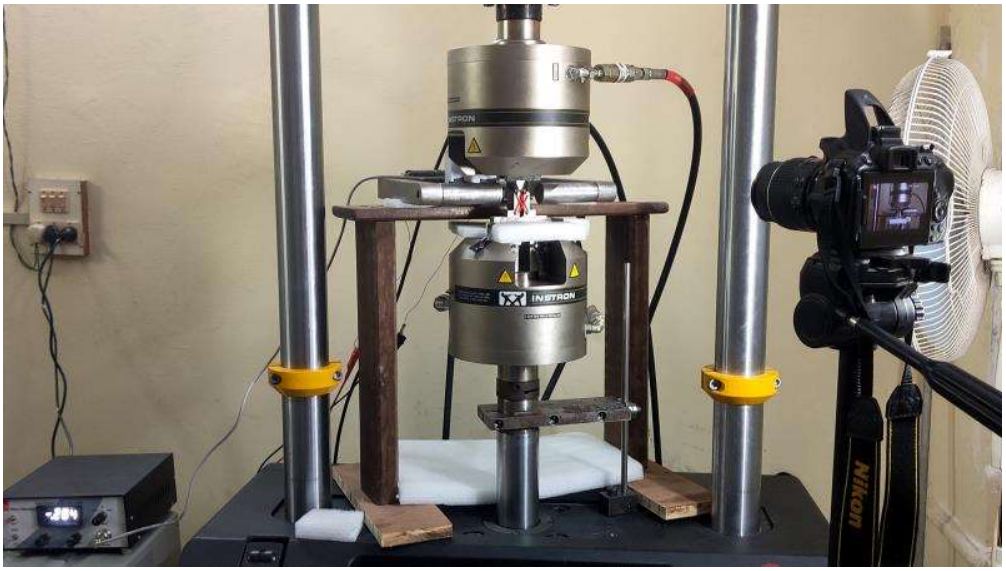

Figure 7.3: DIC setup

Thirty cuboids of Terfenol-D having square cross-section ($3.5\ mm\ \times\ 3.5\ mm$) and length dimension 36 mm are used to prepare the SENB fatigue-fracture specimens. From each cuboid, two fracture specimen are prepared: One to test with the presence of magnetic field and another without it for the characterization of fatigue failure. Hence a total of sixty six specimens are created with a span length of 14 mm as shown in **Figure 7.2**. A high precision wire cut electro discharge machining (Expresscut Ex-4032C) is employed to produce a notch

of 0.5 mm length and 0.1 mm tip radius (**Figure 6.2b**) in the specimen. Considering the high cost of the Terfenol-D material, the dimension and number of specimens are restricted to satisfy the ASTM standards.

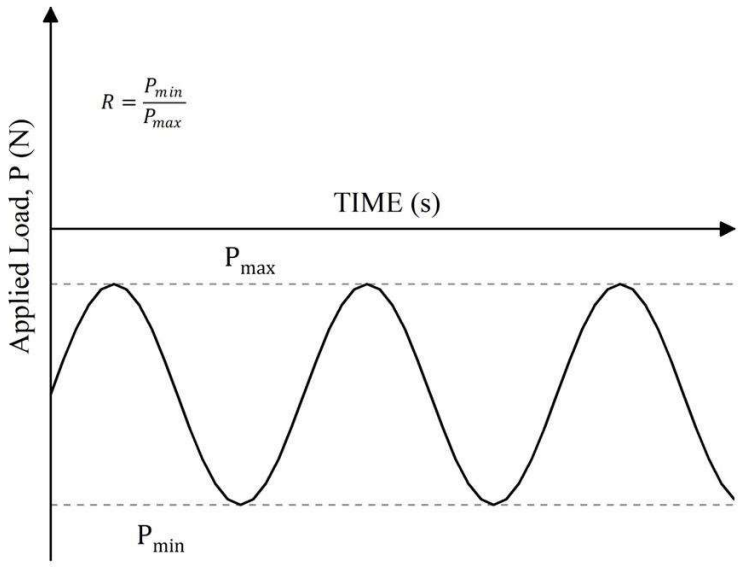

Figure 7.4: Cyclic compressive loading

The specimens are subjected to a sinusoidal loading coaxially to the straight notch at a frequency of $10Hz$ and a constant load ratio of $R = 0.1$ in a cyclic loading procedure as shown in **Figure 7.4**. The load ratio is described as $R = P_{min}/P_{max}$, where P_{min} and P_{max} are the minimum and maximum loads, respectively. Since most Terfenol-D transducers have magnetic operating regimes ranging between 0.02 T to 0.05 T, thus an electromagnet is used to apply a homogenous external magnetic field of magnetic induction ($B_o = 0.03\ T$) in the longitudinal direction of the specimen. All the fatigue experiments are performed in two stages: (1) 15 specimens are tested in cyclic fatigue loading (with maximum load $P_{max} = -40\ N$ and load ratio $R = 0.1$) to capture the fatigue crack growth data with number of spent cycles. Out of which eight samples are tested in presence of the magnetic field and remaining seven in absence of magnetic field. The experimental results for the specimens cross the 40,000 cycles in the presence of magnetic field and the specimens cross the 80,000 cycles in

the absence of magnetic field are considered and remaining data is discarded. (2) In this stage, total fifty specimens are tested in cyclic fatigue loading up to fracture. Out of which 25 specimens are tested with magnetic field and remaining 25 without magnetic field at five randomly distributed levels of maximum load (P_{max}). Thus, five samples are tested for each maximum load level in presence and absence of magnetic field and the number of cycles up to failure are noted. The crack growth data are collected utilising digitalized image correlation software and continuous image capturing with a high-resolution camera set up attached to the 64-bit INSTRON UTM 8801 as shown in **Figure 7.3**. **Figure 7.5** shows the mode I fatigue crack growth from notch in uniaxial cyclic compression at room temperature. All the mechanical tests are carried out with an additional 5kN load cell (resolution of 0.001 N) and measurements are noted in the Bluehill 3 interface. The deformation measurement between two subsequent intervals of the increasing force is close to 5×10^{-5} mm, which demonstrates the measuring precision of the equipment.

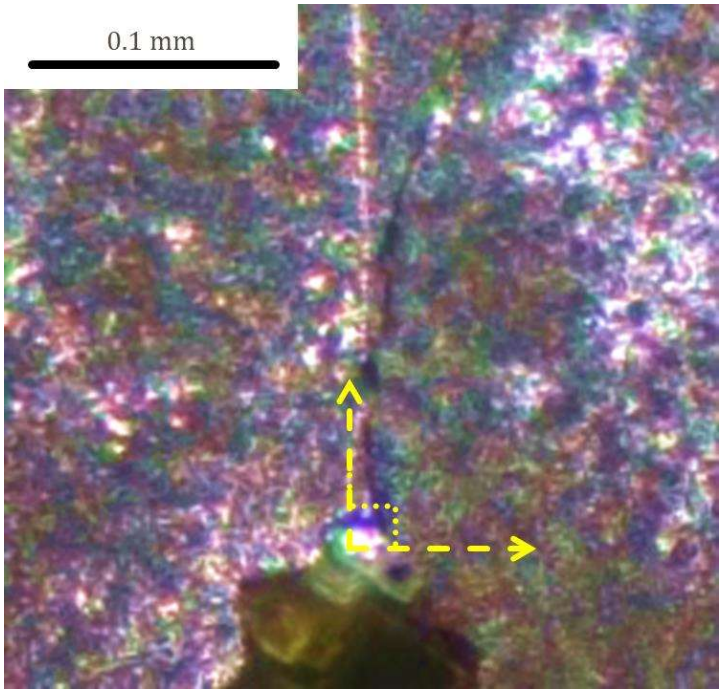

Figure 7.5: Mode I fatigue crack in Terfenol-D specimen

7.3. Numerical model

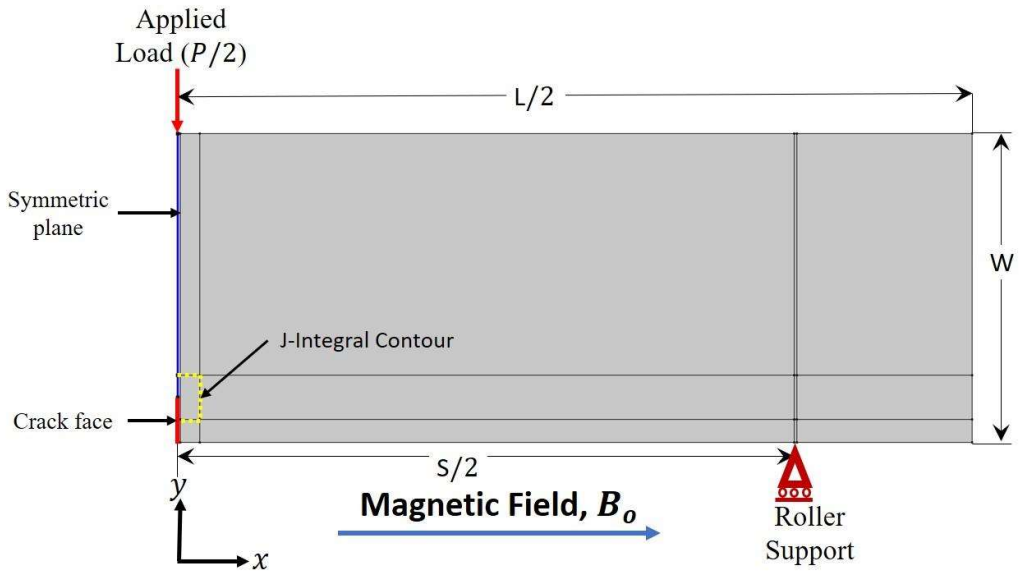

***Figure 7.6**: Half symmetric 2-D FE model for single edge specimen in three-point bending*

In order to evaluate the fatigue-fracture parameters of the Terfenol-D SENB specimen under an applied external field, a 2-D plane strain finite element model of the specimen has been created as similar to the experiment based on the ASTM E399. The governing magneto-elastic field equations and solution methodology is remained same as described in Chapter 5. **Figure 7.6** depicts the half symmetric 2-D FE model that was built for the numerical investigation of the edge-cracked SENB fracture specimen to account for the symmetry of geometry, loading, and support condition. Symmetry conditions are imposed on the sectioned boundaries of the SENB specimen (shaded in blue colour in **Figure 7.6**). It is worth noting that all the traction components are zero along the crack faces, implying that the free boundary condition is met.

A reasonably sized half-symmetric air domain is constructed around the specimen to accurately simulate the magnetic flux path as shown in **Figure 7.6**. The solutions for the differential Maxwell equations given in a domain can be determined by using the appropriate boundary conditions associated with that domain. For a source current free interface between

two mediums having relatively high and low permeability respectively as shown in **Figure 6.6**, then the boundary conditions can be written as [70,71]

$$\hat{\boldsymbol{n}} \cdot (\boldsymbol{B_1} - \boldsymbol{B_2}) = 0 \tag{7.1}$$

$$\hat{\boldsymbol{n}} \times (\boldsymbol{H_1} - \boldsymbol{H_2}) = 0 \tag{7.2}$$

Since the external magnetic field is applied in the direction of perpendicular to the crack surface, thus the boundary condition mentioned in Eq. (7.2) applies at crack surface. In the present analysis, the modelling domain possess magnetic symmetry, then we can reduce the model size to minimize the computational efforts and time. We can exploit the symmetry and interfacial magnetic boundary conditions to truncate the modelling domain. On antisymmetric interfacial plane, the perfect magnetic conductor boundary condition as shown in **Figure 6.7 (b)** presents a condition that strictly requires the tangential component of the magnetic field to be zero so that the magnetic field only points normal to the interface boundary and does not change sign as we pass it. This condition can be written in form of magnetic field as $\hat{\boldsymbol{n}} \times \boldsymbol{H} = \boldsymbol{0}$**.** In case of zero current density, this boundary condition can be described in the form of magnetic scalar potential as $\varphi_m = 0$ [24,72–75] ahead of the crack faces (i.e., on the sectioned boundary in specimen) on the antisymmetric planes. Infinite element domains are employed to minimize the influence on the field in the vicinity of the specimen due to the boundary condition imposed on its remaining exterior boundaries.

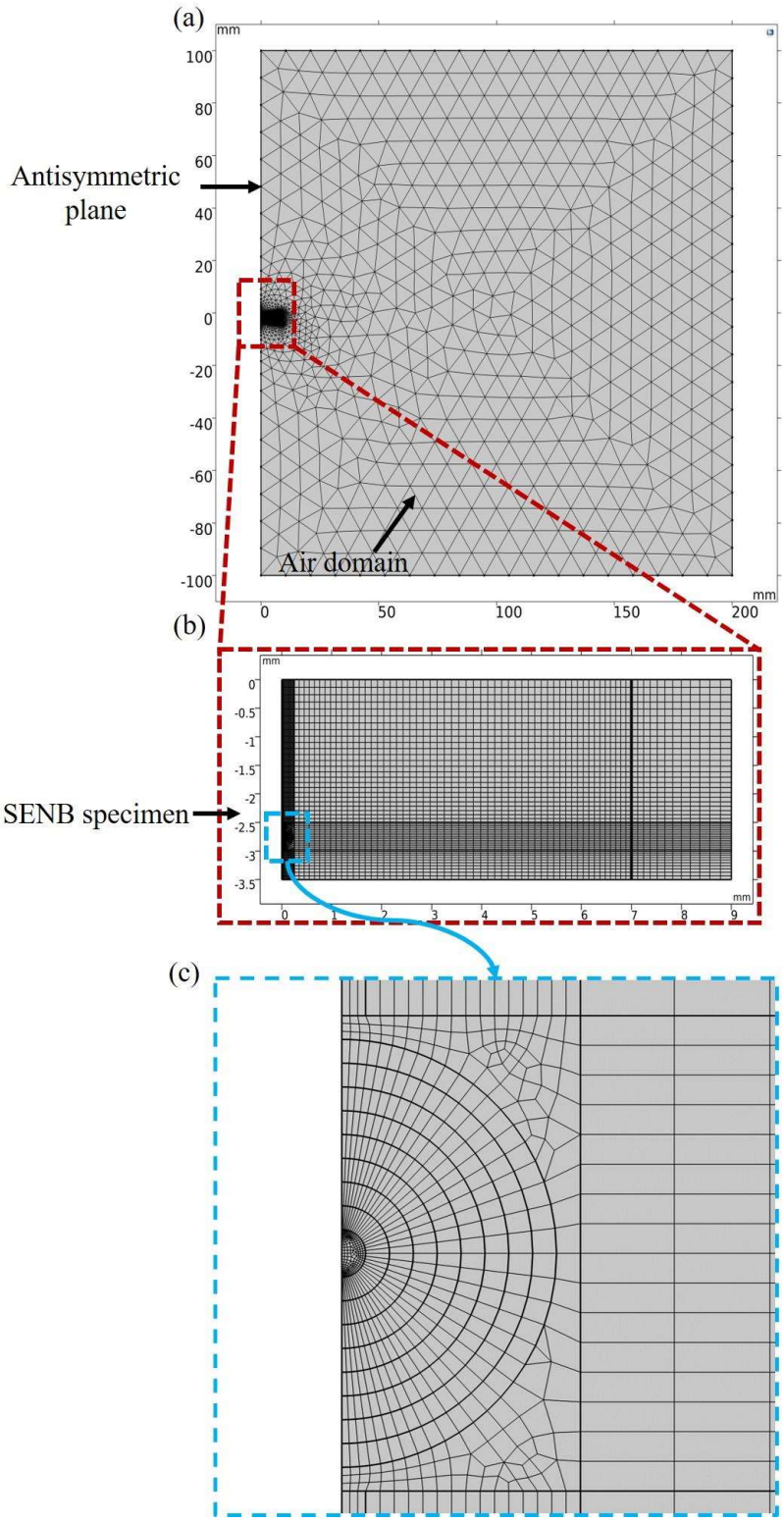

Figure 7.7: FE mesh distribution for the half symmetric numerical model of the single edge three-point bend specimen under the externally applied magnetic field (a) air domain comprising the specimen (b) half symmetric numerical specimen (c) enlarge view of mesh near the crack tip

Figure 7.7 (a) illustrates the FE meshing of the quarter-symmetric numerical specimen as well as the circumambient air domain. A pertinent mesh convergence analysis is conducted to optimize the accuracy of the FE model predictions and the computational effort and time. The meshing of the numerical specimen illustrated in **Figure 7.7 (b)** typically comprises 4922 quadrilateral elements generated using the mapped meshing. Scientifically prudent mesh grading and refinement were performed near the crack tip area to observe the singularity in the stress field, as shown in **Figure 7.7 (c)**. The air domain that meets the numerical specimen is meshed with 4314 triangular elements. **Figure 7.8** shows the direction of the uniform and constant external magnetic field of intensity 0.03 T.

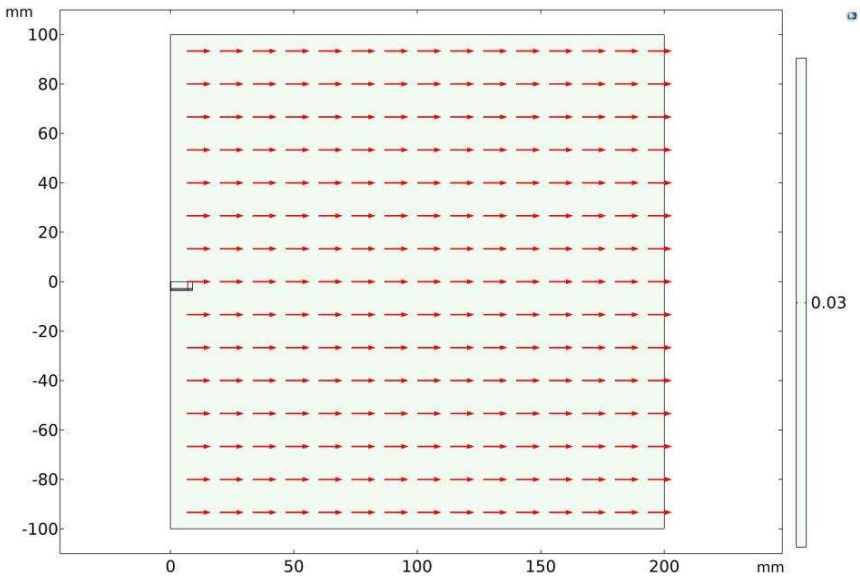

Figure 7.8: Direction of constant external magnetic field ($B_0 = 0.03\ T$)

7.3.1. Computation of *J*-Integral

Terfenol-D has a substantially lower tensile strength than its compressive strength and in the presence of manufacturing flaws or cracks it is susceptible to in-service failures. In addition, Terfenol-D shows high brittleness with no plasticity effects throughout the crack propagation process, a nonlinear elastic analysis should be enough to describe the phenomenon. The nonlinear stress field formulation at the fracture process zone to measure the crack

propagation behaviour may be too complex for use in the fundamental design of intelligent devices. But considering the unprecedented uncertainty in high-risk intelligent device applications, a catastrophe may be better planned if a certain level of reliability preceded the computational effort involved. The final form of the derived 2-D J-integral (Eq. (4.24)) is used to estimate the critical energy release rate (J_{Ic}).

$$J_1(s)_{2D} = \int_{\Gamma}\left[\mathcal{W}^e n_1 - \sigma_{ij} n_j u_{i,1}\right] d\Gamma + \int_{A_1}\left[\sigma_{ij}\left(\frac{\partial \varepsilon_{ij}^n}{\partial X_1} + \frac{\partial \varepsilon_{ij}^m}{\partial X_1}\right) + \left(\rho \ddot{u}_i - M_j \frac{\partial B_{0i}}{\partial X_j}\right) u_{i,1}\right] dA \tag{7.3}$$

The half symmetric numerical specimen with a single edge notch of length 'a' is subjected to three-point cyclic bending as described in previous section (**Figure 7.6**). The quadrilateral elements are implemented across the crack front. The ensuing deformation in the specimen is functionally reliant on the stress characteristics and the distribution of magnetization. In the ongoing numerical simulation, the x and y-directions correspond to the X_1 and X_2 co-ordinates, respectively. The plane strain J integral is evaluated over a contour traced by yellow dashed lines and area enclosed by that contour as shown in **Figure 7.6**. The line integration operators are defined for the contour and the global expressions of $\int_{\Gamma}\left[\mathcal{W}^e n_1 - \sigma_{ij} n_j u_{i,1}\right] d\Gamma$ are setting up for the calculation of path integration. It is worth noting that the boundaries of the crack front are not included in the J-integral evaluation since all the traction components are zero as the crack faces are not loaded. When computing the J-integral, the normal of contour must point outward of the region which the contour encompasses. To ensure that this is the case, a local normal variable whose sign can be inverted when necessary is defined. The area integration operators are setting up on the area delineated by contour that encloses the crack front, is utilized to evaluate the area integral. The global expressions of area integral $\int_{A_1}\left[\sigma_{ij}\left(\frac{\partial \varepsilon_{ij}^n}{\partial X_1} + \frac{\partial \varepsilon_{ij}^m}{\partial X_1}\right) + \left(\rho \ddot{u}_i - M_j \frac{\partial B_{0i}}{\partial X_j}\right) u_{i,1}\right] dA$ are

established for computation. The accuracy of this coupled physics problem for evaluating nonlinearity in strain distribution iteratively is extremely sensitive to mesh size and dependent on the number of iterations. Due of the nonuniform tension and compression zones, the bi-nonlinear phenomena can certainly be observed in the 3-point bend simulation of the SENB specimen.

7.4. Results and discussions

In this section, the effect of magnetization and the nonlinear elasticity on the fatigue crack propagation is examined. This study process involves the cyclic three-point bend test on SENB fracture specimens to evaluate the fatigue crack extension with respect to number of cycles spent and correspondingly the appropriate numerical simulations to evaluate the updated Paris law constants. Then the life of pre-cracked giant magnetostrictive material samples is predicted numerically and validated experimentally. The following sub-sections explain the observations of the relevant study.

7.4.1. Experimental results for crack growth

In the first stage of experimentation, ten specimens are tested in cyclic fatigue loading with maximum load $P_{max} = -40\ N$ and load ratio $R = 0.1$ to capture the fatigue crack growth data with number of spent cycles. Five samples are tested in presence of the magnetic field and remaining five in absence of magnetic field. The crack growth data are collected periodically and recorded together with the number of cycles by utilising digitalized image correlation technique and continuous image capturing with a high-resolution camera set up attached to the 64-bit INSTRON UTM 8801 as shown in **Figure 7.3**. **Figure 7.9** shows the fatigue crack extension with number of cyclic loading cycles for Terfenol-D SENB specimen according to ASTM E-647. The significant decrement in the crack extension and number of cycles to fatigue-fracture is observed in the presence of magnetic field (0.03 T) when maximum load $P_{max} = -40\ N$. Although number of samples are limited due to

expensiveness of the Terfenol-D but this decrement can be reasoned to increment in the critical strain energy release rate (J_{Ic}) due to the rotation of domains in the presence of applied external magnetic field as discussed previously in Chapter 6.

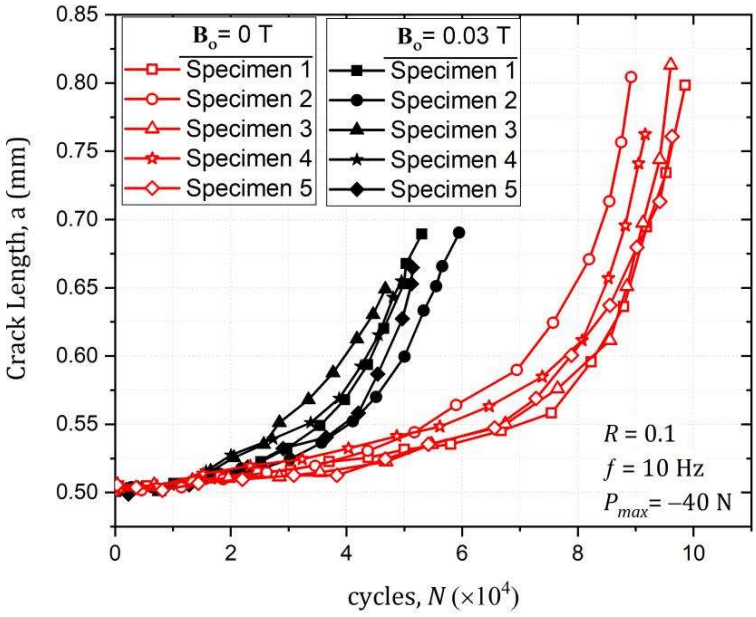

Figure 7.9 Variation of crack advancement vs number of cycles

7.4.2. Numerical determination of updated Paris law constants

Chow et al. [99] explains that the ΔK (as described in Eq. (2.42)) is not sufficient to adequately characterise the fatigue crack growth behaviour in non-linear elastic materials. The strain energy release rate defined by J-integral (i.e., ΔJ) [99–101] can be used as a physically more reasonable quantity than ΔK which is recognised as the crack driving force in nonlinear elastic material. Thus the ΔJ can be considered as the primary source for the essential energy dissipated during fatigue crack growth. The Paris and Erdogan relation can be updated as

$$\frac{da}{dN} = C'\Delta J^{m'} \tag{7.4}$$

Here C' and m' are the equivalent updated Paris law constants. The constants C' and m' can assume number of values according to situation. In above equation, ΔJ can be written as

$$\Delta J = J_{max} - J_{min} \tag{7.5}$$

where, J_{max} and J_{min} can be computed for maximum and minimum cyclic load (i.e., P_{max} and P_{min}, respectively) with the help of Eq. (7.3). Again, a log-log scale can be used to plot the updated Paris curve, with the crack development rate per cycle (da/dN) on the ordinate (y axis) and the cyclic ΔJ amplitude on the abscissa (x axis), respectively.

Thus, to evaluate the updated Paris law constants, it is required to plot crack development rate per cycle of loading (da/dN) with respect to the cyclic ΔJ amplitude on log-log scale from **Figure 7.9** (i.e., crack growth vs number of cycles curve). Then by using the linear curve fitting technique on log-log plot, the constants for updated Paris law can be determined. The slope of crack growth vs number of cycles curve (i.e., $da/dN \approx \Delta a/\Delta N$) can be determined for any crack length by secant or point-to-point method recommended by the ASTM E-647. The secant approach for measuring the crack extension rate includes computing the slope of the straight line joining two neighbouring data points on the crack length vs number of cycles graph as described in **Figure 7.10**. It can be expressed as

$$\left(\frac{da}{dN}\right)_{a_{avg}} = (a_{i+1} - a_i)/(N_{i+1} - N_i) \tag{7.6}$$

Here, the measured (da/dN) is an average rate over the $(a_{i+1} - a_i)$ increment. The average crack length $a_{avg} = (a_i + a_{i+1})/2$ is used to evaluate the ΔJ with the help of Eq. (7.3).

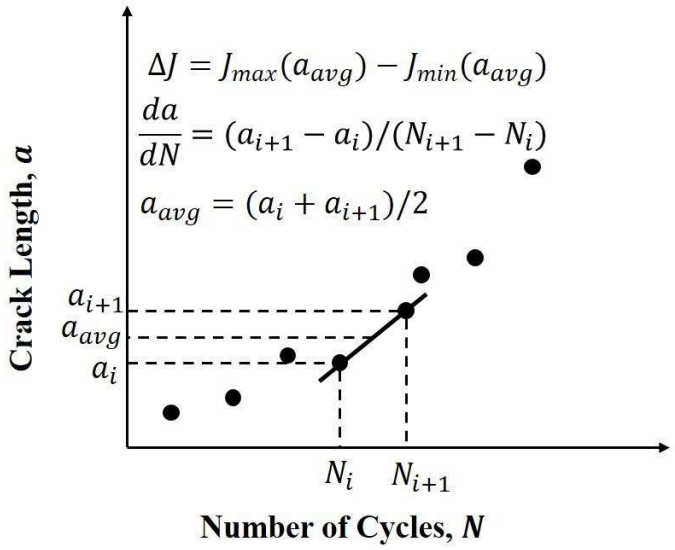

Figure 7.10: Determination of slope of curve at any random point by secant method

The crack driving force ΔJ can be computed by following the algorithm as shown in **Figure 7.11**. This algorithm is implemented in a finite element method based tool (i.e., COMSOL Multiphysics) for one mechanical loading cycle to compute ΔJ. The J-integral can be evaluated as described in section 7.3.1. The main solution steps of the approach are briefly described here:

Step 1: Parametrize the average crack length (a_{avg}) in the geometry of numerical specimen as shown in **Figure 7.6**.

Step 2: Vary the average crack length data from initial crack length to final crack length (i.e., up to fracture) using the parametric sweep feature in COMSOL Multiphysics for both cases, i.e., with the presence of magnetic field and without the magnetic field.

Step 3: Find the nonlinear stress field solution for every average crack length data using the algorithm as shown in **Figure 5.3** for coupled field loading in both cases, i.e., with the presence of magnetic field and without the magnetic field.

Step 4: Compute the ΔJ for upper and lower levels of the cyclic load i.e., P_{max} and P_{min}.

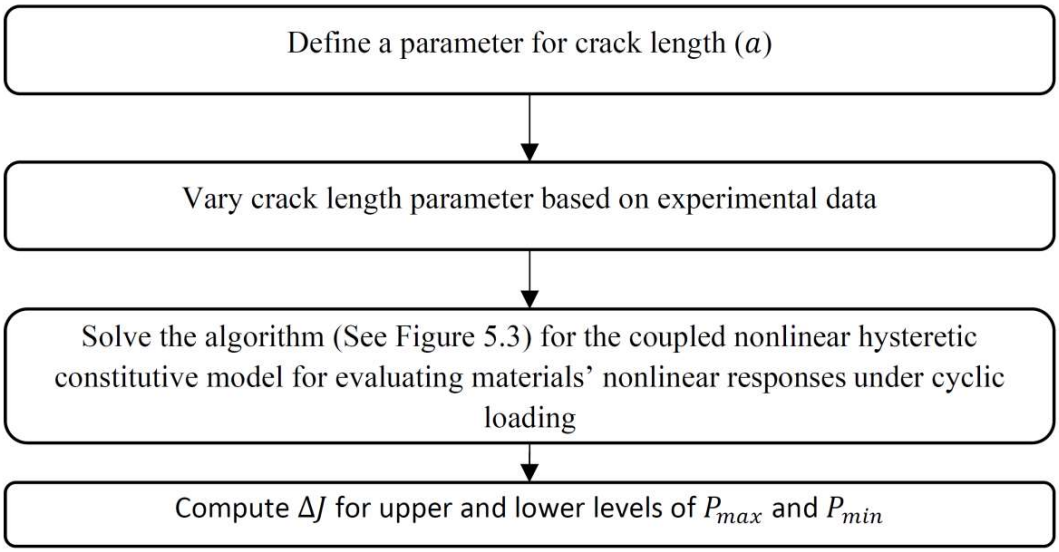

Figure 7.11: Numerical scheme for evaluation of ΔJ with the variation in crack growth

Figure 7.12 and **Figure 7.13** show the Von-Mises stress distribution and the magnetization pattern in the numerical specimen of Terfenol-D at a maximum cyclic load of -40 N with an applied field of 0.03T, respectively. It is readily evident from the Von-Mises stress illustration that the singular stresses are present in the vicinity of the crack front. The simulated graph of magnetization distribution (**Figure 7.13**) demonstrates that the specimen's magnetization adheres to distinct values depending on whether it is in the tensile or compressive zone. This phenomenon is attributed to the change in magnetic anisotropy produced by flexure stresses in positive magnetostrictive materials. The changes in magnetic anisotropy can be explained based on the magnetic domain rotations. Precisely, the flexure tensile stresses tend to align the spin distributions parallel to the longitudinally applied magnetic field; consequently, magnetization saturation occurs faster. In contrast, the flexure compressive stresses tend to orient them in a plane at right angles to the longitudinal direction; thus, the magnetization process becomes more arduous. As illustrated in **Figure 7.13**, the magnetization values approaching saturation near the crack front region reaffirm the consistency of the domain analysis.

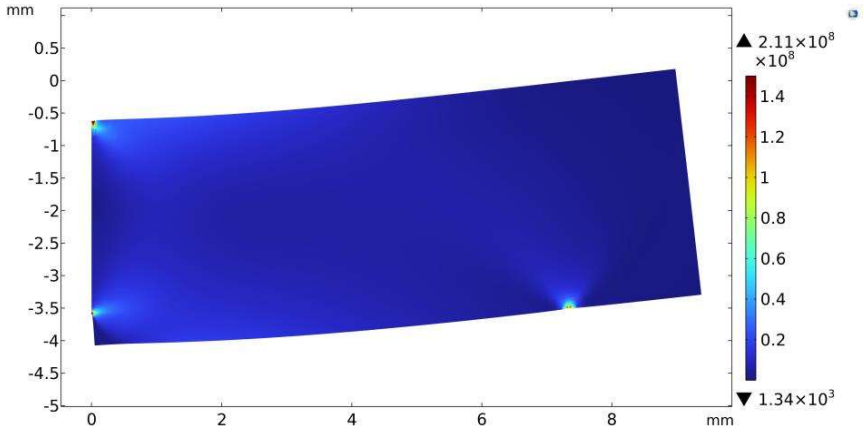

Figure 7.12: Von mises stress (in Pa) distribution in the half symmetric Terfenol-D specimen at 0.03 T subjected to -40 N

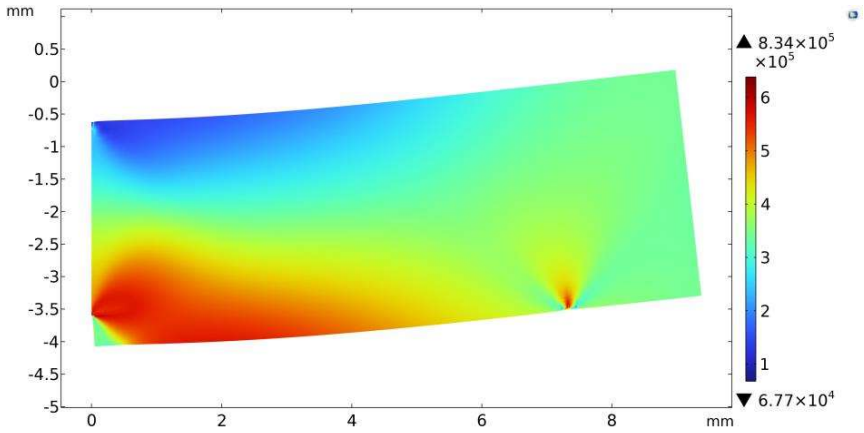

Figure 7.13: Magnetization norm (in A/m) distribution in the half symmetric Terfenol-D specimen at 0.03 T subjected to -40 N

Figure 7.14 depicts the tensile and compressive zones in the midplane of the numerical specimen at a maximum cyclic load of -40 N with an applied field of 0.03T. **Figure 7.15** shows the effect of the magnetic field on the stress field distribution in the numerical specimen of Terfenol-D with and without an applied field of 0.03T. The stress field distribution is plotted at the same load level (i.e., -40 N) in both the absence and presence of a magnetic field for comparison purposes. An increment in the stress field is seen when a magnetic field of 0.03 T is applied. This change can be visualized more clearly near the crack tip in the zoomed-view plots of each case.

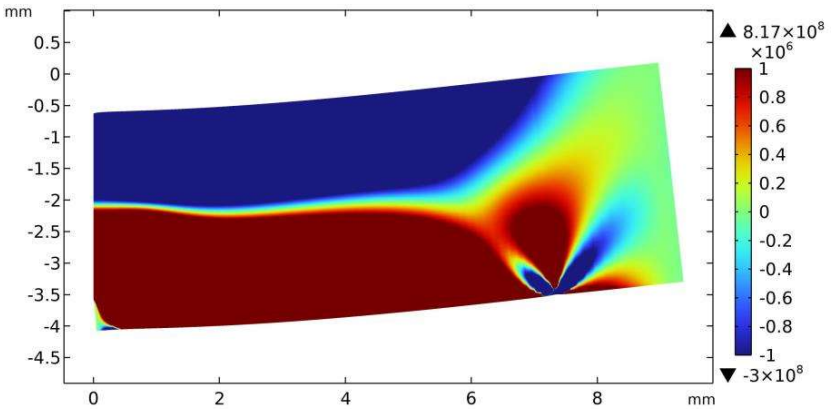

Figure 7.14: Stress (in Pa) component in x-direction distribution in the half symmetric Terfenol-D specimen at 0.03 T subjected to -40 N

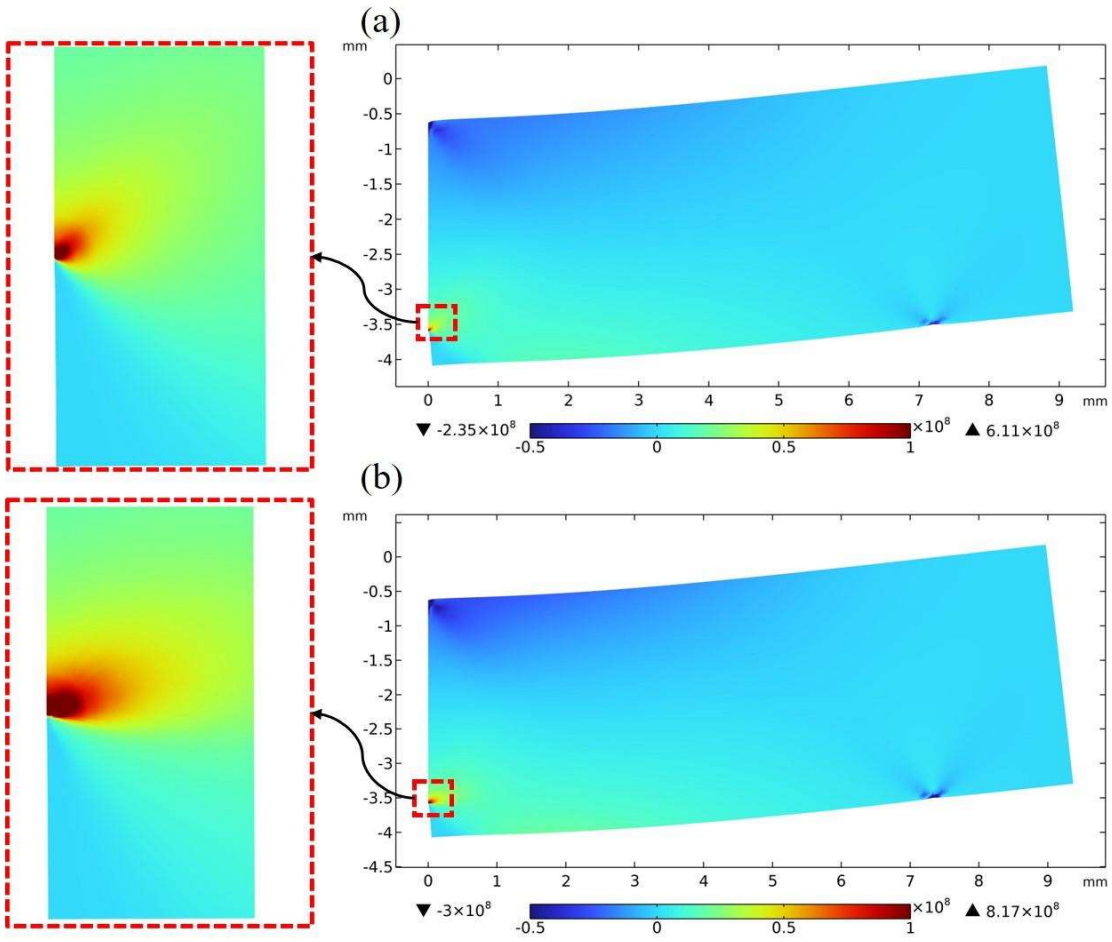

Figure 7.15: Comparison of stress (in Pa) component in x-direction distribution in the numerical specimen when subjected to load -40 N (a) in absence of magnetic field (b) in presence of 0.03 T magnetic field.

Figure 7.16 shows the crack development rate per cycle of loading (da/dN) with respect to the cyclic ΔJ amplitude plot on the log-log scale. The sensitivity of growth rate (da/dN) to the change in strain energy release rate range ΔJ in presence of magnetic field, is markedly higher than that in absence of magnetic field. The linear curve fitting technique on the log-log plot is used to determine the constants for updated Paris law. The updated Paris law for the Terfenol-D specimens at load ratio $R = 0.1$ and frequency $f = 10\,Hz$ in presence of magnetic field 0.03 T can be determined as

$$\frac{da}{dN} = 1.84 \times 10^{-21}(\Delta J)^{12.43} \tag{7.7}$$

and the updated Paris law for the Terfenol-D specimens at load ratio $R = 0.1$ and frequency $f = 10\,Hz$ in absence of magnetic field can be determined as

$$\frac{da}{dN} = 2.18 \times 10^{-15}(\Delta J)^{8.58} \tag{7.8}$$

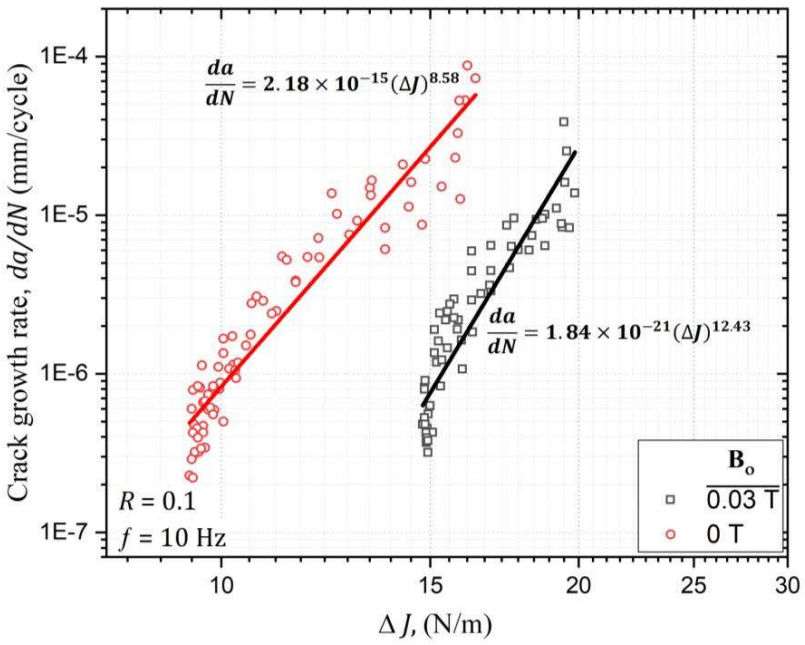

Figure 7.16: Fatigue crack growth rate as a function of strain energy release rate range ΔJ

These equations can be used to predict the life of the Terfenol-d specimen in fatigue loading with and without the applied magnetic field. Each Terfenol-D SENB specimen fails when ΔJ becomes equal to critical ΔJ_{cr}. The value of ΔJ_{cr} is computed for each specimen from the 2-D plane strain finite element method using Eq. (7.3). The average value of ΔJ_{cr} is obtained as 14.80 N/m and 18.61 N/m in the presence of magnetic field (0.03 T) and absence of magnetic field, respectively, which is consistent with the numerical results of 2-D J_{Ic} values as shown in Table 6-4, although data is very limited as more specimens are necessary to get proper results. Furthermore, if we computed the average value of ΔJ_{cr} with the help of 3-D J-integral, then the difference in the average value of ΔJ_{cr} may not be that significant (i.e., found almost identical in Table 6-4) as we evaluated in the 2-D plane strain analysis. This difference may be due to the fact that, while the plane-strain state is thought to be met near the crack-front at the mid-plane of the finite thick specimen, the actual stress-strain state in the specimen differs from that in an infinite thick specimen. The detailed discussion regarding to this phenomenon given in section 6.5.3. However, despite of the above benefits of the three dimensional assessment of crack tip singularity, we limited this study to 2-D plane stain assessment due to limitation of the computing facility. It will take more than year to solve this problem.

7.4.3. Numerical fatigue life prediction and experimental validation

This section is dedicated to numerical evaluation of the fatigue-fracture load data with the number of cycles spent for Terfenol-D SENB specimens at load ratio $R = 0.1$ and frequency $f = 10\ Hz$ in the presence of magnetic field (0.03 T) and absence of field with the help of updated Paris law Equations (7.7) and (7.8), respectively. The most efficient approach for this numerical simulation is to start by setting up the coupled magneto-elastic problem in the graphical user interface of the COMSOL Multiphysics. The nonlinear stress field solution for any crack length parameter (a_i) can be computed using the numerical algorithm as shown

in **Figure 5.3** for one mechanical loading cycle in coupled field environment. This algorithm (**Figure 5.3**) is implemented in a COMSOL Multiphysics model as described in section 5.3.1 and 6.3. Then, the *.mph model file (i.e., COMSOL model file) can be easily loaded into MATLAB by using the COMSOL-MATLAB live link feature. Further a script based on the **Figure 7.17** (i.e., numerical scheme for evaluation of fracture load data with the number of cycles spent) is implemented in MATLAB to create a model M-File for solving the model. The J-integral can be evaluated as described in section 7.3.1.

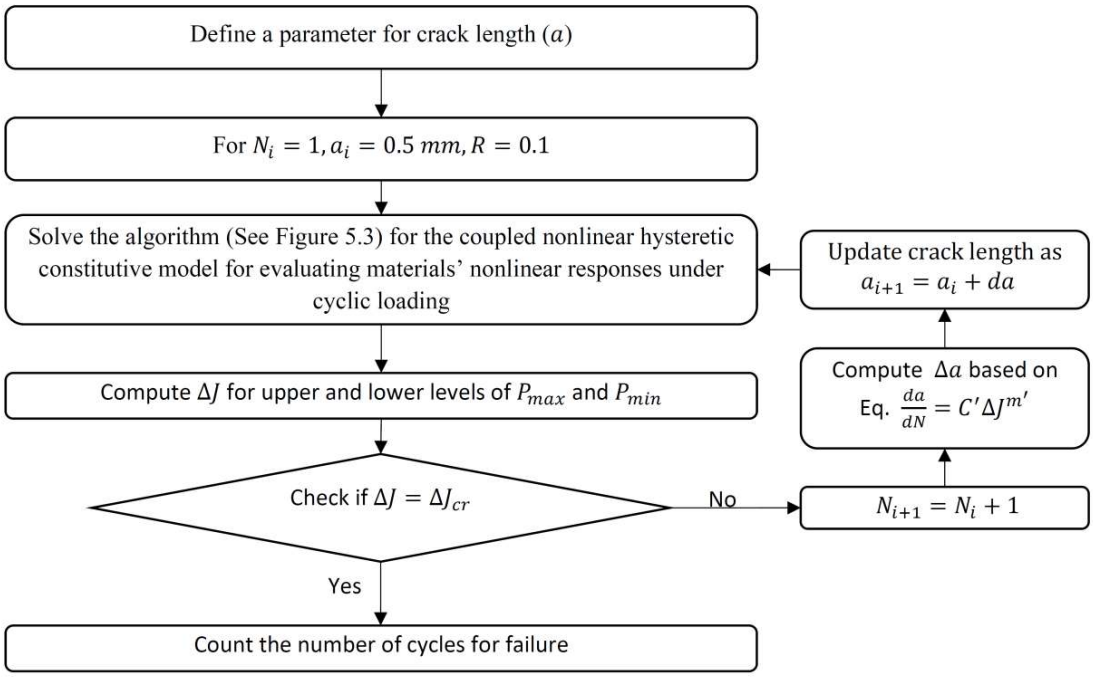

Figure 7.17: Numerical scheme for evaluation of fracture load data with the number of cycles spent

The main solution steps of the approach implemented in MATLAB are briefly described here:

Step 1: Define a parameter for the crack length (a) in the geometry of numerical specimen as shown in **Figure 7.6**.

Step 2: Initiate the fatigue loading loop for first loading cycle as $N_i = 1, a_i = 0.5\ mm, R = 0.1$.

Step 3: Find the nonlinear stress field solution for crack length data (a_i) using the algorithm as shown in **Figure 5.3** for one mechanical loading cycle in coupled field environment.

Step 4: Compute the ΔJ for upper and lower levels of the cyclic load i.e., P_{max} and P_{min}.

Step 5: Check whether ΔJ is equal to critical ΔJ_{cr} or not. If $\Delta J \neq \Delta J_{cr}$ then update the fatigue loading cycle count as $N_{i+1} = N_i + 1$ and compute the change in crack length Δa with the help of updated Paris law Equations (7.7) and (7.8), in the presence of magnetic field (0.03 T) and absence of field, respectively. Then update the crack length as $a_{i+1} = a_i + da$. Now input the updated crack length data in Step 3 to recompute the ΔJ. This process goes on until the fatigue fracture condition $\Delta J = \Delta J_{cr}$ is met.

Step 6: However, if $\Delta J = \Delta J_{cr}$, then stop the computation and count the total number of loading cycles.

The numerical life of Terfenol-D SENB samples predicted for a number of different maximum cyclic loading levels P_{max}. The P_{max} levels used in the presence of magnetic field (0.03 T) are 38 N, 39 N, 41 N, 42 N, 43 N, 44 N and 45 N and in absence of magnetic field are 41 N, 41.5 N, 42 N, 44 N, 46 N, 48 N, 49 N and 50 N. The average value of ΔJ_{cr} is used in numerical prediction as 14.80 N/m and 18.61 N/m in the presence of magnetic field (0.03 T) and absence of magnetic field. The predicted life in terms of number of spent cycles are shown in **Figure 7.18**.

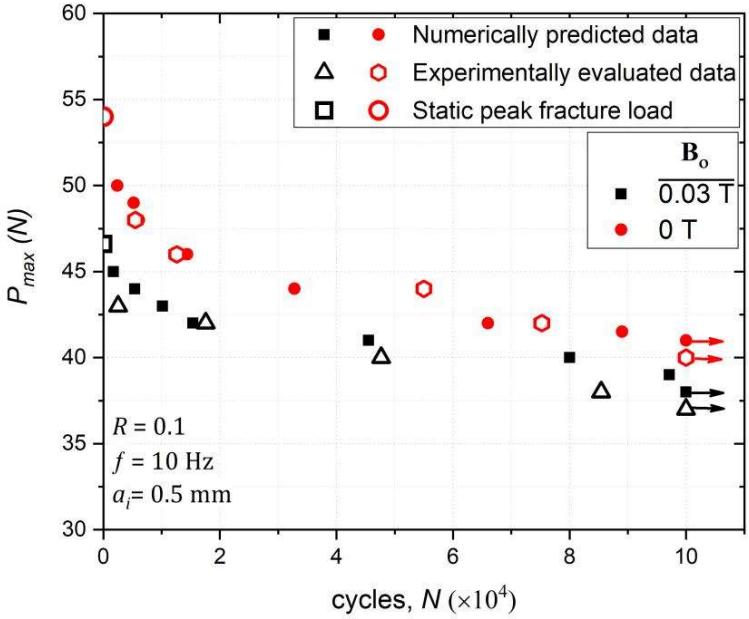

Figure 7.18 Maximum load versus number of cycles to failure of Terfenol-D

To validate the numerical approach described to predict the fatigue life of Terfenol-D SENB specimen, an experimental analysis is performed. In this analysis, total fifty specimens are tested in cyclic fatigue loading up to fracture. Out of which 25 specimens are tested with magnetic field and remaining 25 without magnetic field at five randomly distributed levels of maximum load (P_{max}). Thus, five samples are tested for each maximum load level in presence (i.e., 37 N, 38 N, 40 N, 42 N and 43 N) and absence (i.e., 40 N, 42 N, 44 N, 46 N and 48 N) of magnetic field and the number of cycles up to failure are noted in **Table 7-1** and **Table 7-2**, respectively. The average values of the number of cycles up to failure are plotted in **Figure 7.18** and the data for specimens that did not fracture after 10^5 loading cycles are shown by an arrow adjacent to the data point. As well **Figure 7.18** also shows the mean of static peak fracture load data from Table 6-2 for quasistatic three-point bend fracture test in magneto-elastic field.

Table 7-1: Fatigue-fracture load data in presence of the magnetic field 0.03 T.

Maximum load (P_{max})	**Specimen Number**	**Number of spent cycles before fracture**
43 N	Specimen 1	4128
	Specimen 2	1523
	Specimen 3	3524
	Specimen 4	1205
	Specimen 5	2235
	Average	**2523**
42 N	Specimen 1	10929
	Specimen 2	27685
	Specimen 3	15857
	Specimen 4	12753
	Specimen 5	20586
	Average	**17562**
40 N	Specimen 1	53657
	Specimen 2	38956
	Specimen 3	49576
	Specimen 4	33425
	Specimen 5	62831
	Average	**47689**
38 N	Specimen 1	84251
	Specimen 2	73694
	Specimen 3	97526
	Specimen 4	79829
	Specimen 5	91825
	Average	**85425**
37 N	Specimen 1	98527
	Specimen 2	115325
	Specimen 3	104977
	Specimen 4	102854
	Specimen 5	121752
	Average	**108687**

Table 7-2: Fatigue-fracture load data in presence of the magnetic field 0.03 T.

Maximum load (P_{max})	**Specimen Number**	**Number of spent cycles before fracture**
48 N	Specimen 1	5297
	Specimen 2	6732
	Specimen 3	6752
	Specimen 4	2436
	Specimen 5	6283
	Average	**5500**
46 N	Specimen 1	9874
	Specimen 2	14527
	Specimen 3	11330
	Specimen 4	11458
	Specimen 5	15741
	Average	**12586**
44 N	Specimen 1	68542
	Specimen 2	46957
	Specimen 3	57864
	Specimen 4	51276
	Specimen 5	50896
	Average	**55107**
42 N	Specimen 1	74297
	Specimen 2	81468
	Specimen 3	71493
	Specimen 4	64439
	Specimen 5	84528
	Average	**75245**
40 N	Specimen 1	117651
	Specimen 2	105887
	Specimen 3	101752
	Specimen 4	124561
	Specimen 5	117969
	Average	**113564**

It can be seen from **Figure 7.18** that the experimentally evaluated fatigue life data of Terfenol-D SENB specimens demonstrates good consistency with the numerical prediction.

The maximum cyclic load values required to fail the specimen falls sharply with respect to the static load values as this steep decrement can be reasoned to the combined mechanical and magnetic hysteresis effects in the Terfenol-D specimen. The number of cycles to fracture failure increases as the maximum load on the Terfenol-D specimen lowers. Furthermore, with an applied magnetic field $B_0 = 0.03$ T, the number of cycles required for the failure of Terfenol-D SENB specimens is less than the number of cycles required when a magnetic field is not applied, even though the data is relatively sparse.

7.5. Summary

In this chapter, a combined theoretical and experimental study has been conducted to understand the influence of magnetic fields on the cyclic fatigue behavior of Terfenol-D. The number of cycles to failure of Terfenol-D under magnetic fields was smaller than that under zero magnetic field when identical load, load ratio and cycle frequency conditions are maintained. By using the finite element techniques, a log-log plot is created between the sensitivity of the growth rate (da/dN) and strain energy release rate range ΔJ. Then, by linear curve fitting techniques, the updated Paris law for the Terfenol-D specimens under fatigue loading at load ratio $R = 0.1$ and frequency $f = 10\ Hz$ in the presence and absence of magnetic field are determined. The sensitivity of growth rate (da/dN) to the change in strain energy release rate range ΔJ in the presence of a magnetic field is markedly higher than in the absence of a magnetic field. The numerical fatigue life of Terfenol-D SENB specimens is predicted for different maximum cyclic load levels. An experimental analysis is conducted to validate the predicted numerical life. The numerically evaluated data for fracture loads with the number of cycles spent show a good agreement with the experimentally evaluated data.

This Page is Intentionally Left Blank